J. Fluid Mech. (2007), *vol.* 587, *pp.* 347–372.
doi:10.1017/S0022112007007331 Printed in the United Kingdom

Shear-weakening of the transitional regime for granular flow

KEVIN LU[1], E. E. BRODSKY[2] AND H. P. KAVEHPOUR[1]

[1]Department of Mechanical and Aerospace Engineering, University of California, Los Angeles, Los Angeles, CA 90025, USA

[2]Department of Earth and Planetary Science, University of California, Santa Cruz, Santa Cruz, CA 95064, USA

(Received 6 September 2006 and in revised form 11 May 2007)

This paper experimentally investigates the rheology of dense granular flow through its solid-like to fluid-like transition. Between the well-established flow regimes – quasi-static and grain-inertial – the physical description of the transition remains elusive. Our experiment uses a top-rotating torsional shear cell capable of $\pm 1\,\mu m$ accuracy in height and 5 decades ($10^{-3} - 100\,rad\,s^{-1}$) in rotation rate. The data on beach sand shows that shear and normal stresses exhibit an inverse rate-dependence under a controlled volume environment in the transitional regime, while in the limiting regimes the results are in agreement with previous work. The shear-weakening stresses illustrate a previously unknown 'dip' with increasing shear rate. Under a controlled-pressure environment, however, the shear-compacting volume-fraction 'peaks' with increasing shear-rate. We combine these results from both configurations to infer a constitutive law based on a rate-invariant granular fluid compressibility. The formulation provides an equation-of-state for dynamic granular systems, with state variables of pressure, strain rate and free-volume-fraction. Fitting parameters from independent constant-volume and constant-pressure data shows good agreement in validating our model. Moreover, the degree of grain jaggedness is essential to the rate-dependence within the transitional regime. The results on the solid–fluid transition may elucidate the evolution of granular flow anisotropies.

1. Introduction

Under continuous strain, granular material display regimes analogous to all three phases of matter, i.e. solid, liquid and gas (see Jaeger, Nagel & Behringer 1996). These phases have distinct modes of momentum transfer between grains under different amounts of external excitations – surface shear, air injection or vibration. With small excitations and little or no confinement, granular material escapes from a jammed state into a mobilized one (see Cates, *et al.* 1999; O'Hern, *et al.* 2001; Corwin, Jaeger & Nagel 2005). Within this regime, the long-duration grain-to-grain interaction is frictional Coulomb-type with momentum exchanging mainly through rubbing and rolling. The interactions often involve many grains in aggregated forms (see Savage, *et al.* 1983; Savage 1984) within this rate-independent quasi-static regime (QS). With increasing excitation, granules can achieve a readily flowing phase. Like the molecules in a dilute gas, particles within this grain-inertial regime (GI) interact predominantly through short-duration binary collisions (see Savage, *et al.* 1983). Similar to an ideal

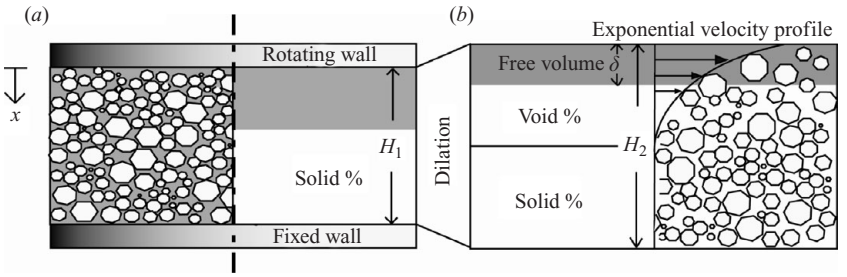

FIGURE 1. Schematic of static and dynamic regimes of granular flow. (*a*) The static volume of column height H_1. Shaded and unshaded regions indicate volumetric void and solid fractions, respectively. (*b*) The shaded region shows the 'free' volume expanded from static packing. The total height is H_2 and the dilation constant is δ. The exponential velocity profile has been observed previously. The effective void fraction ϕ is the ratio between the dynamic free expanding volume and the original static volume. The diagram is not drawn to scale.

gas within this dynamic state, GI stresses are quadratically rate-dependent. A modified kinetic theory has been used to describe the underlying physics behind highly agitated granular materials (see Savage 1998). Between the two extreme regimes – GI and QS – however, there exists a transition flow that has yet to be empirically defined.

Studies have formulated both computational and theoretical results on the dynamics of granular flow (see Bagnold 1954; Savage 1984; Hanes & Inman 1985; Jop, Forterre & Pouliquen 2006). Other authors have studied granular rheology and its dependencies on shear rate, volume-fraction, gravity and applied pressure (see Campbell 1990; Karion & Hunt 1999; Hsiau & Shieh 2000; Klausner, Chen & Mei 2000; Tardos, McNamara & Talu 2003; Bossis, Grasselli & Volkova 2004). Specifically, constitutive equations for shear and normal stresses have been hypothesized for granular hydrodynamics (see Savage 1998; Bocquet *et al.* 2002; Hendy 2005). However, the physics behind the transition between GI and QS regimes have mostly been overlooked, despite theoretical uncertainties (see Tuzun *et al.* 1982; Bocquet *et al.* 2002) and anomalous empirical data signalling its peculiarities (see Tardos, Khan & Schaeffer 1998; Dalton *et al.* 2005). Experiments have indicated that both contact force distribution (see Corwin *et al.* 2005; Dalton *et al.* 2005) and geometrical anisotropy (see Majmudar & Behringer 2005) evolve within a sheared granular system under intermediate deformation rates. The collective effect of these local flow phenomena on the grain scale escalates the complexities of granular dynamics.

In this study, we explore shear rates that span all three dynamic flow regimes: grain-inertial, transitional and quasi-static. We perform laboratory experiments with both natural beach sand and milled quartz grains in a torsional shear rheometer where the rotational velocity is varied systematically over 5 orders-of-magnitude. We then compare the rheological results from constant-stress and constant-volume configurations to address granular compressibility. To study the effects of flow anisotropy and force network, two different grain column heights are used (figure 1). Sample sphericity is also observed to affect granular flow greatly and result in an unexpected shear-weakening behaviour. Moreover, a model is devised based on granular compressibility that retains Coulomb yield conditions and granular dilatancy. From fitting the model to the experimental data, we find consistent parameters in support of our equation-of-state for non-thermal non-attractive particle systems. By doing so, we may have captured the experimental ramifications of localized flow

phenomenon – the formation and collapse of clusters and force chains – as a self-organized resistance to granular deformation.

2. Dimensionless rate

Bagnold (1954) was the first to classify granular flows in a liquid medium. Savage and others later narrowed their efforts to dry systems and quantified their experiments with the Savage number (see Savage 1984),

$$Sa = \frac{\rho D^2 \dot{\gamma}^2}{\sigma}. \tag{2.1}$$

The Savage number is the ratio between inter-granular collisional stress and consolidation stress, and it is intended to delineate QS, GI and transition flow regimes. Parameter ρ is particle density, D is mean grain diameter, $\dot{\gamma}$ is shear rate, and σ is consolidating stress. Note the consolidation force includes all compacting forces such as gravity or electro-static forces if present.

From visually observing the experiment, we suspected that the shear-band thickness – the mobilized region of grains – remained independent of rate. Others have made similar observations for confined torsional flows (see Savage & Sayed 1984; Karion & Hunt 1999; Tardos *et al.* 2003). Visual measurements on the velocity profile are made at $50\,\mathrm{rad\,s^{-1}}$ and $0.01\,\mathrm{rad\,s^{-1}}$ recorded at 1000 f.p.s. and 1 f.p.s., respectively. Particle-tracking data were fitted to an exponential profile $u(y)$ of

$$u(y) = U_R \exp\left(-\frac{y}{L}\right), \tag{2.2}$$

where U_R is the rim velocity and L is the characteristic flow depth. The resulting fit at both velocities yields $L \approx 2D$, where D is the mean grain diameter. In contrast, in free-surface or avalanche flows driven by gravity, the characteristic flow depth geometry depend on channel width or tilt (see Jop, Forterre & Pouliquen 2005).

From the rate-invariant characteristic depth of $\approx 2D$, we infer that the rate-independent shear flow thickness is of order $\sim D$. With this constraint, the Savage number (2.1) then becomes grain-size independent of the form

$$Sa = \frac{\rho U^2}{\sigma}. \tag{2.3}$$

3. Experiment set-up and procedure

In the present experiment, we investigate the connection between stress, volume-fraction and strain rate over a wide range of deformation rates ($\sim$5 decades). Our objective is to understand the granular flow regimes, with an emphasis on the transition regime and its elusive rheological properties. Using a torsional rheometer shown in figure 2, we intend to study particle flows governed by purely repulsive and frictional interactions. The varying parameters in our experiment are top-plate height, angular velocity and pressure, while material properties, i.e. rigidity and average grain size, are fixed. Dependencies on polydispersity and sphericity, although not substantially examined, are discussed in the context of our model and interpretation.

To analyse accurately a system of discrete mobilized particles, it is vital to account for the following inherent features of granular materials: compressibility; segregation; crystallization; and packing configurations. First, the compressible nature of the particle 'fluid' warrants two different experimental procedures: constant-volume and

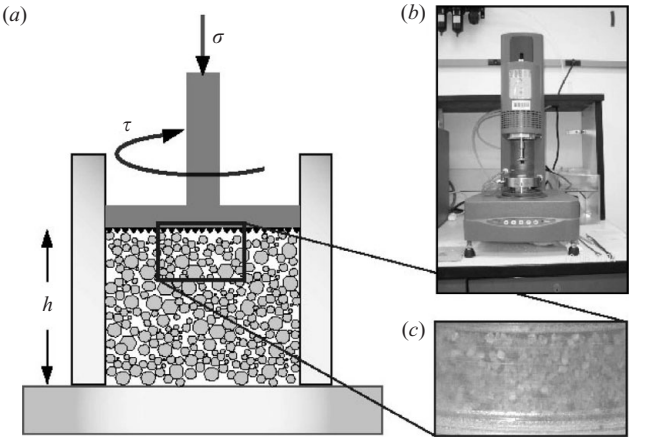

FIGURE 2. Illustration of torsional shear cell. (*a*) The experimental set-up using a cylindrical shear cell with a radius of 10 cm for lateral confinement. (*b*) Rheometer TA Instruments AR-2000. (*c*) Actual photograph of the polydisperse beach sand used as the sample. The top surface transmits shear through a taped 80 grit sand paper. The granular medium has a random packing solid volume-fraction $\nu \approx 0.59$. The instrument measures and controls τ, σ, H and the rotation rate from the top-plate boundary. Angular velocity ranges from 10^{-3} to $10^{2}\,\mathrm{rad\,s^{-1}}$ which corresponds to 10^{-5} to $1\,\mathrm{ms^{-1}}$ at the rim.

constant-pressure (see § 3.2 for discussion). In contrast, compressibility is insignificant for the rheology of conventional liquids.

Secondly, segregation occurs within granular systems of different grain sizes (see Makse *et al.* 1997; Shinbrot 2004). Polydispersity – grain mass variance – in our rotational device, in response, creates an inertial stress gradient in the radial direction. The stress gradient then segregates large grains to the rim away from smaller grains near the centre. To investigate the impact of this segregation effect on our results, we performed the same experiments on beach sand with and without sifting.

Thirdly, crystallization occurs within systems of spherical particles where abrupt changes occur at the liquid–crystal cross-over (see Drake 1990). To avoid this transition and to sustain an amorphous state at low or zero shear rates, therefore, the chosen polydispersed sample must have irregular jagged shapes. Thus, we choose samples of angular beach sand and spherical F-35 foundry sand (US Silica Co.) to show sphericity effects on granular rheology. Figures 3(*a*, *b*) and table 1 summarize the properties of the three samples – sifted sand, unsifted sand and US Silica F-35 – used in our experiments.

Lastly, there exist many meta-stable configurations, or stackings, of any given set of particles depending on the loading history (see Campbell 2005). These meta-stable packing configurations arise from the frictional nature of interacting grains, where the smallest perturbation in the magnitude or the direction of the compressive stress can disrupt this fragile arrangement (see Liu & Nagel 1998). One implication of this fragility is material compaction: granular packing increases its solid volume-fraction when subjected to vibration or deviatoric strain (see Duran 1999). Thus in our experiment, we anneal each granular sample from a pre-experimental shear until there is no compaction within the experimental time scale of hours.

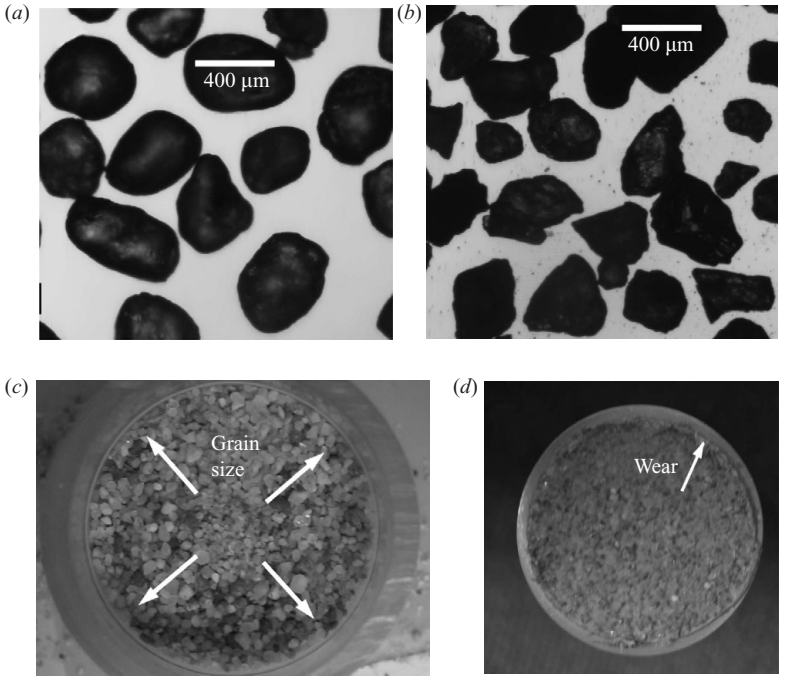

FIGURE 3. Micrographs of actual grains using KP-D50 (Hitachi). Samples used are (*a*) US Silica F-35 foundry sand, and (*b*) beach sand. The two samples show large sphericity differences but with similar averaged size. Photographs using a Canon PC1060 camera show (*c*) surface size segregation of unsifted sand after reaching steady state and (*d*) shear surface wear near the edge of the 20 mm diameter sandpaper after 10 experiments.

Properties	Sifted beach sand	Unsifted beach sand	US Silica F-35
Material	Quartz/lithic	Quartz/lithic	Silica quartz
Density ($\mathrm{kg\,m^{-3}}$)	2650	2650	2650
Shape	Angular	Angular	Quasi-spherical
Diameter range (μm)	197–1142	47–2000	282–1142
Mean diameter (μm)	438±188	458±255	530±152
Static volume-fraction	≈0.61	≈0.61	≈0.62

TABLE 1. Sample properties. Sifted beach sand preparation uses US standard. mesh size 18 and 120, with respective opening sizes of 1000 μm and 125 μm. US Silica F-35 is prepared from the factory. The beach sand originated from life guard tower 9, Santa Monica, CA, and it is stored at room temperature and humidity. Grain-size and variance data are acquired using laser diffraction (Beckman–Coulter particle-size analyser).

3.1. *Instrument set-up and sample preparation*

To investigate the granular flow, we use a torsional rheometer (AR-2000, TA Instruments). As seen in figure 2, the system has an upper rotating plate with 20 mm diameter and a lower fixture that can detect normal force (± 0.1 N) through an internal force transducer. The rheometer is a highly sensitive feed-back controlled instrument that simultaneously monitors torque, normal force, top-plate height and angular velocity.

Traditionally, the system is used to study the rheological behaviour of conventional fluids. In our application, the upper plate is used for compression either by controlling normal stress (± 1 Pa) or plate height ($\pm 1\mu$m), while shearing through a user-specified velocity range. The upper plate has taped 80 grit (300 μm sand grains) sandpaper to facilitate stress transmission. Tape is also set on the bottom fixture to gain traction. To contain the grain sample, a Teflon self-lubricating sleeve, with a thickness of 0.4 cm is concentrically aligned around the shearing plate. Although the sidewall friction is unavoidable, the system can be rotationally mapped to counter all of the external resistance by applying a background torque. During optimal alignment, the experiment achieves an average sidewall stress contribution of $\approx 1\%$ of the total shear stress. An annulus set-up with concentric inner and outer walls has been considered, but all attempts failed to reduce wall friction to below 10% of the overall stress. Sidewall flex/stretching is not of concern for stress variations of $\sim 10^3$ kPa for a rigid cylindrical sleeve.

The samples used in these experiments are natural and sifted beach sand and US Silica F-35 foundry sand, all of which are composed of grains that are highly rigid and irregular in shape (table 1 and figure 3*a*, *b*). The sifted beach sand is prepared by sieving the sample through a US standard mesh size 18 and 120, respectively, with 1000 μm and 125 μm openings. US Silica F-35 is sieved from the factory. The beach sand is predominantly quartz (>70%) with small quantities of lithics and other minerals while the US Silica sample is entirely quartz. These materials have a Young's modulus of 30—70 GPa and thus they are highly rigid compared to our experimental stresses of $\sim 10^3$ Pa. Other relevant sample properties are given in table 1. The reference volume-fraction is measured by weighing the samples after compaction with light tapping. Grains examined post-experimentally do not show changes in polydispersity and sphericity.

3.2. *Procedure*

To begin, the granular sample is loaded up to one of two heights: 1 mm and 6 mm that correspond to roughly 3 and 20 grain diameters, respectively. Although there are large 1 mm grains in the 1 mm columns, shape irregularities and surface roughness ~ 300 μm allow smaller grains to contact the top and bottom surfaces. The reason for using the 3-grain column is, according to numerical simulations of Tardos *et al.* (2003) and experimental observations by Hanes & Inman (1985), that 10 to 13 grain diameter is the 'effective' shearing zone in a granular layer because of the exponential decay of the velocity with depth discussed in § 2. The result from a 3-diameter column would therefore pinpoint the effect of an inadequate shear zone; an effect of shallow inter-grain force-propagation on the stress-rate relationship (see de Gennes 1999; Majmudar & Behringer 2005).

After loading the granular sample, the granular layer is pre-sheared for ~ 100 rotations to make the packing consistent. Then during every experiment, the sample is sheared from fast to slow at logarithmically distributed velocities. Slow-to-fast experiments have similar results, as will be shown in figure 6. (The shearing surface does not degrade significantly during high shear rates but after 8–10 runs, degradation eventually produce erratic results.) During shear, the sampling rate for shear/normal stress and column height is 10 Hz. Other experimental parameters, i.e. velocity range and averaging times, are given in table 2. Generally, the chosen velocity range stays above rates that result in stick–slip (see Aharonov & Sparks 2004) and below rates that promote excessive wear on the top-plate sandpaper as shown in figure 3(*d*).

System parameters	Constant volume	Constant pressure
Column heights	1 to 12 mm	–
Pressures	–	1 to 7 kPa
Velocity step 1	0.001–0.01 rad s^{-1} (300 s)	
Velocity step 2	0.01–1 rad s^{-1} (180 s)	
Velocity step 3	1–100 rad s^{-1} (30 s)	

TABLE 2. Control parameters of constant volume and constant pressure procedures. The column height is user-specified at 10 rad s^{-1} for a particular pressure during constant volume procedures. The pressure is user-specified during constant pressure procedures. The velocity steps and their range use different data averaging times, indicated in parentheses. Each logarithmic decade has 6 to 10 data points.

To account for granular compressibility, two general shearing conditions are used: constant volume and constant pressure. In the constant-volume procedure, the specified column height stays fixed while the instrument varies pressure and rate. The specified column height is system-determined from a pre-experimental procedure of fixed pressure (10^4 Pa) and velocity (10 rad s^{-1}). The reason is because of volume-dilatancy, the column height in the constant-volume procedure must be set while the grains are mobilized. In this configuration, the granular volume-fraction remains constant. The second shearing condition is a constant-pressure configuration. A user-specified normal stress ($\sim 10^3$ kPa) is feedback-controlled by adjusting the column height, resulting in changes of volume-fraction as a function of shear rate. Both constant-volume and constant-pressure procedures have a fixed numbers of particles.

4. Results and discussion

A torsional shearing device can achieve a large torsonial strain but cannot accurately capture the rate-dependent rheology of non-Newtonian fluids. The drawback is that the shearing velocity become a function of the radius, r, measure from the centre. In the context of granular flow, the issue is that the flow is always quasi-static in the centre even if the rotational velocity is extremely high. The measured stress is therefore an averaged stress $\langle \sigma \rangle$ given as

$$\langle \sigma \rangle = \frac{2\pi}{A_{disk}} \int_0^R \sigma(r) r \, \mathrm{d}r.$$

We therefore need to approximate the Savage number in (2.3) with caution. We remedy this issue by computing an effective linearized velocity $U = \omega R^*$ using the stress-centroid to find R^* as

$$\mathrm{R}^* = \frac{\int_{disk} \mathrm{r}(\tau \, \mathrm{dA})}{\int_{disk} \tau \, \mathrm{dA}}, \tag{4.1}$$

where r is radius and dA is the infinitesimal disk area. Then the Savage number from (2.3) becomes

$$Sa = \frac{\rho(\omega R^*)^2}{\sigma}, \tag{4.2}$$

where $(2/3)R \leqslant R^* \leqslant (4/5)R$, ω is angular velocity and R is the shear plate radius. Within the rate-dependent GI regime, the constant factor is 4/5 rather than 2/3 because the inertial stresses vary with radius as $\sim \mathrm{r}^2$. Therefore the velocity (4.2)

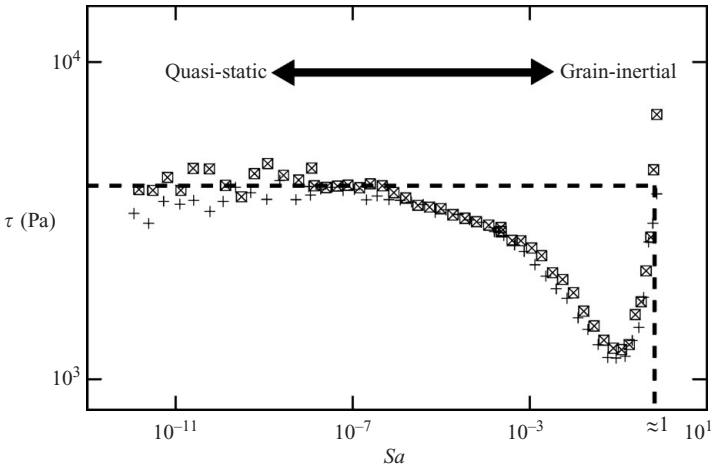

FIGURE 4. Log–log plot of shear stress versus the Savage number of ≈1 mm column. Both experiments have the same column heights and similar pressures. The Savage number is calculated at the transition into both grain-inertial and quasi-static regimes to be $Sa \sim 1$ and $Sa \sim 10^{-7}$, respectively. ⊠, 3298 pa; +, 3075 pa.

under-estimates the equivalent linear velocity, and thereby reduces the Savage number, in the GI regime. The analysis also disregards the effects of secondary flow, with its velocity gradient in the radial direction. Hanes & Inman (1985) have used similar assumptions to interpret their torsional shear cell results.

4.1. *Constant-volume experiment*

Figure 4 outlines the flow regimes to be presented. The GI regime begins around $\omega = 25\,\mathrm{rad\,s^{-1}}$ and the conversion using (2.3) and (4.2) results in $Sa \sim 1$ at this velocity. The QS regime and its non-trivial transition into the GI regime is also observed. Figure 4 is reminiscent of the powder flow diagram of Tardos *et al.* (2003) depicting various granular flow regimes. Using our parameters, the dimensionless rate used in Tardos *et al.* (2003) and Klausner *et al.* (2000) also results in $U/(gD)^{1/2} \sim 1$ and the consistency between the two dimensionless rates validates the present flow regimes.

4.1.1. *Grain-inertial (GI) and quasi-static flow (QS)*

In figure 5(*a*), the shear stress is plotted against angular velocities through a range of 10^{-3} to $10^{2}\,\mathrm{rad\,s^{-1}}$. They correspond to a Savage number of the order of 10^{-11} to 1. The two limiting regimes – GI and QS – can be identified easily for all three samples via visual inspection where the stresses are rate-independent and quadratically rate-dependent, respectively. To fit our results, a power-law is used

$$\tau = \tau_0 + \tau_1 \omega^n \quad \text{or} \quad \tau = \tau_0 + (\tau_1 C)\dot{\gamma}^n, \tag{4.3}$$

where ω is the rotation rate, $\dot{\gamma}$ is the shear rate at the wall and τ_0 , τ_1 and C are rate-independent fitting parameters.

Our power-law fit yields a nearly quadratic stress-rate relationship similar to many experimental and theoretical results, showing a quadratic stress dependence on shear rate (see Savage 1984; Savage & Sayed 1984; Hanes & Inman 1985; Karion & Hunt 1999; Klausner *et al.* 2000). From figure 5(*a*, *b* insets), the rate-dependent shear stress within the grain-inertial regime for polydispersed beach sand is observed. The rate-dependence is nearly quadratic, i.e. $n \approx 2$, for both shear and normal stresses,

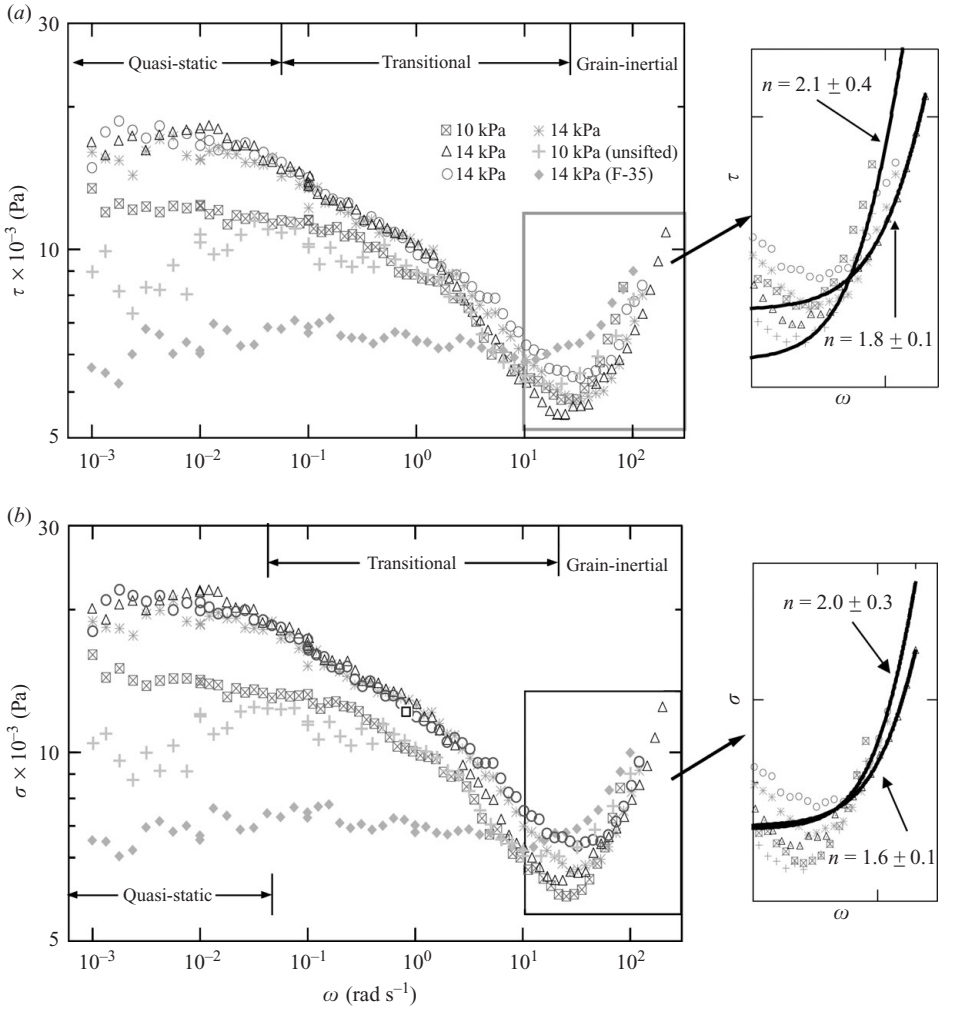

FIGURE 5. Log–log plot of wall stresses versus rate at constant volume and ≈6 mm columns. (*a*) Shear stress τ versus angular velocity ω. Average normal stresses σ_{avg} uses all pressure data of a single run. (*b*) Normal stress σ versus angular velocity ω. The insets (F-35 not shown) show the power-law exponent fitted to the data along with the coefficient n in (4.3). The standard deviation values are based on 100 bootstrap trials. Sifted sand is used unless noted. Unlike beach sand, F-35 foundry sand of higher sphericity does not weaken in the transitional regime. The column height is between 6 mm and 12 mm for all runs which exceeds the mobilized regions of ≈10 grain diameters; thus instead of column-height, averaged pressures label each run in the legend.

but the lack of GI data results in large standard deviation values of ∼0.1 computed from boot-strapping. The present experiment agrees with previous work that yielded a range of powers, n, between 0.75 and 2 for the grain-inertial stresses (see Savage 1984; Klausner *et al.* 2000; Sawyer & Tichy 2001; Tardos 2003).

All three flow regimes are revealed for a medium with a single volume-fraction. In contrast to the conclusion drawn by Campbell (2002), it is possible to obtain the GI and the QS regimes from an equally dense medium. In our case, the volume-fraction

of statically packed sand is ≈0.61, slightly less than the maximum random close packing for spheres of ≈ 0.64.

4.1.2. *Transitional flow*

In figure 5(*a*, *b*), both shear and normal stresses are inversely proportional to shear rate within the transitional regime using unsifted and sifted beach sand. Three runs with sifted sand at average pressure ∼14 kPa uses identical parameters to show consistency. One additional run with sifted sand at ∼10 kPa shows the dependence of pressure: pressure induces shear-weakening since stresses dip less under smaller pressures. Unsifted sand at ∼10 kPa shows minimal grain segregation effects where shear-weakening during intermediate rates matches well with sifted sand at the same pressure. At a higher sphericity, however, US Silica F-35 sheared at ∼14 kPa does not weaken during the same transitional velocity range. Average pressures are based on the entire velocity range. In addition to figure 5, figure 6 shows repeatability of the current results for unsifted sand and F-35 as well as results from slow-to-fast shearing.

Here we offer a simple model to show that the shear-weakening phenomenon is not an artefact of the torsional geometry – namely the non-uniform shear rate that depends on radius – and that a similar stress-rate relationship would occur in a linearized shear flow. Following § 4.1.1 and (4.3), we assumed that

$$\tau = \tau_0 + \tau_1 C \left(\frac{\omega R^*}{L} \right)^2 \quad \text{for } \dot{\gamma} \sim \frac{\omega R^*}{L}, \tag{4.4}$$

where R^* is derived in (4.1) and L is the characteristic length from (2.2). By simply separating the total stress into frictional and kinetic parts, this model, similar to previous work (e.g. Savage 1984), can only predict a monotonic increase τ with rate ω. This is not what we observed. The shear-weakening transitional flow cannot be generated from (4.4), thus it must be intrinsic to the rheology of a granular fluid, rather than to any geometrical artefacts.

The exact physics behind the weakening is unknown. However, we offer a qualitative explanation: the observed pressure-induced shear-weakening in granular systems elucidates the evolution of its force network. As shown by Ostojic, Somfai, & Nienhuis (2006) under large loads, the fractal medium adapts to external stresses by aligning strong contacts into filamentary force chains. This stress-induced anisotropy also exists geometrically (see Majmudar & Behringer 2005) where the filamentary chains physically align to the direction of the externally applied shear stress. These adaptive chains can then resist shear by carrying ≈10 times the mean external stress (see Corwin *et al.* 2005). Together, in response to stress, the force-chain formation can be interpreted as a self-organizational stiffening of granular materials.

As rate increases, grain interactions become more collisional and less frictional (see Corwin *et al.* 2005). Instead of prolonged contacts, these rapid collisions reduce spatial anisotropy and hence decrease its resistance to shear. This force network breakdown is then illustrated by the shear-weakening transition. As seen in figure 5(*a*, *b*), under constant volume, the dissimilar stresses within the transitional regime seem to converge when approaching the GI regime, for pressures of 10 and 14 kPa. This trend indicates the diminishing effect of contact force anisotropy with increasing shear; a consistent interpretation that leads to a more uniform (ergodic) kinetic GI regime where grains take on binary collisions. A similar shear-thinning rheology is common in dense hard-core colloidal fluids (see Larson 1999).

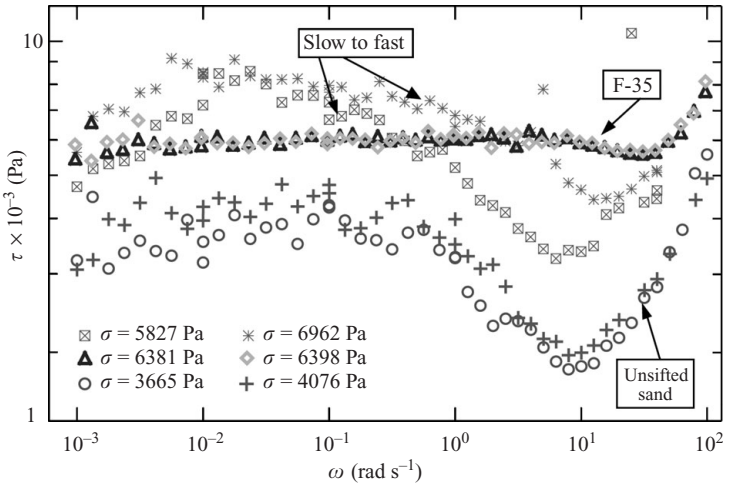

FIGURE 6. Log–log plot shear stress versus angular velocity at constant volume ($H \approx 6$ mm). Similar to fast-to-slow experiments in figure 5(*a*), slow-to-fast experiments show transitional shear-weakening rheology. Samples F-35 and unsifted sand experiments shows repeatability in extension to figure 5(*a*).

Another crucial feature arises in the comparison between beach sand and US Silica F-35 where shear weakening is not observed for the latter (also in figure 6). In this case, we explain that samples with different degrees of sphericity have different packing preferences. In general, because of the 'caging' effect – mobility hindrance by neighbouring particles – angular grains flow less easily than spherical grain samples (see Yu *et al.* 1996; Zou & Yu 1996; Larson 1999). As seen in figure 5, under the same average pressures, lower shear and normal stresses are observed for F-35 than for beach sand. Flowing with perhaps local crystallized regions (see Drake 1990), the self-organized stiffening mechanism possible for angular beach sand is entirely avoided by spherical F-35. In hindsight, O'Hern *et al.* (2003) have also suggested that a mixture of highly angular particles is required to explore the entire granular phase space.

The above interpretations may explain the absence of the transitional regime from earlier simulations and experiments. Other concentric shear cells use gravity as the consolidating pressure of the order of 10^2 Pa at mid-height for a 10 cm column (see Bocquet *et al.* 2002; Tardos *et al.* 2003; MiDi 2004). Insufficient gravity forces, together with perhaps uncontrolled volume, may not induce the same structural responses as explained here. Similarly, simulations using perfect spheres with varying rigidity can (see Campbell 2005; da Cruz *et al.* 2005) recover only the rate-independent transition regime as indicated by our quasi-spherical F-35 samples.

The shear-weakening transition is shown to be almost insensitive to sample polydispersity by the sifted sand results in figures 5 and 6. This is consistent with a configuration where the stresses are transmitted vertically between relatively monodispersed particles. Driven by the rotating plate, segregation occurs by grains exerting centripetal forces directed outward in the radial direction. As shown in figure 3(*c*), this outward inertial force circumferentially aligns equal-sized grains near the shearing surface with larger grains separate from smaller ones. As grains segregate by size, the colliding particles in adjacent horizontal layers are relatively mono-dispersed. Therefore a torsional cell may reduce, or even eliminate, the effect of

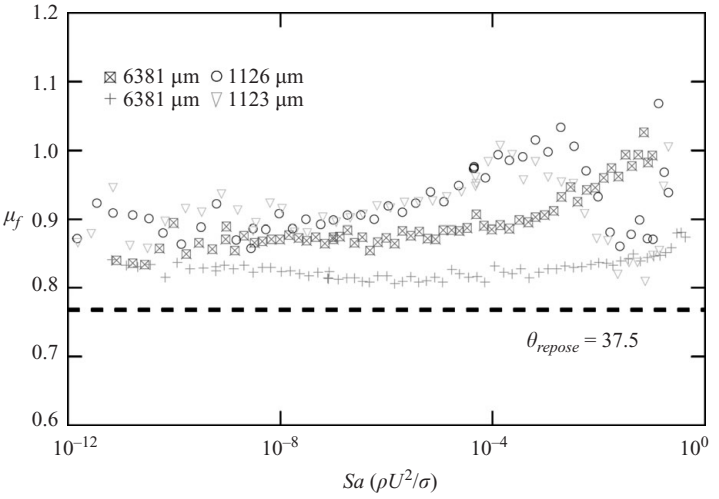

FIGURE 7. Semi-log plot showing coefficient of friction versus the Savage number for beach sand in a constant-volume experiment. The plot compares experimental data from high- and low-shear column-heights. The higher height runs exceed the shear-band thickness of ≈10 grain diameters. The lower height has ≈3 grain diameters across. θ_{repose} is the angle of repose measured from the slope of a static granular pile. The observed increase of the friction coefficient $\mu_f \sim \tan\theta_{repose}$ of all runs compared to the angle of repose of a static pile may indicate the dependence of the friction coefficient on volume-fraction. All other runs exhibit a regime-invariant friction coefficient.

polydispersity in steady-state granular rheology. The result supports the assumption of a monodispersed sample that is made to calculate the Savage number in § 2.

We note in passing that the lack of shear-weakening in the US Silica F-35 results also demonstrates that the 'dip' is not an artefact of our torsional device.

4.1.3. *Friction*

In figure 7, we use the constant-volume method to investigate the friction coefficient by plotting the ratio from shear and normal stresses against the Savage number. Not surprisingly, the close resemblance of shear and normal stress behaviour produce a friction that is nearly independent of shear rate. In support of our result, both Savage (1998) and Cheng & Richmond (1978) proposed that normal stress is proportional to the shear stress and independent of how particles interact.

In figure 7, the friction coefficient is compared with the angle of repose, θ_{repose}, of the sample measured from the inclination of a prepared sand pile. The resulting friction coefficientof $\mu = 0.78$, where $\mu = \tan\theta_{repose}$, is about 11% lower than the compressed sand from our shear-flow experiment (see Nedderman 1992). The comparison highlights the mobility hindrance due to confinement where grains under constant volume have less interstitial space than flowing grains near a free surface. The lack of space inhibits grain mobility, thus producing a higher friction coefficient than unconfined flows – the difference is revealed by the intricate filamentary network of force chains explained in § 4.1.2.

4.2. *Constant-pressure experiment*

Figure 8 is a semi-log plot of normalized volume-fraction versus rotation rate from constant-pressure experiments. It is erroneous to report the bulk volume-fraction since only the height change is measured. Thus the normalized volume-fraction is

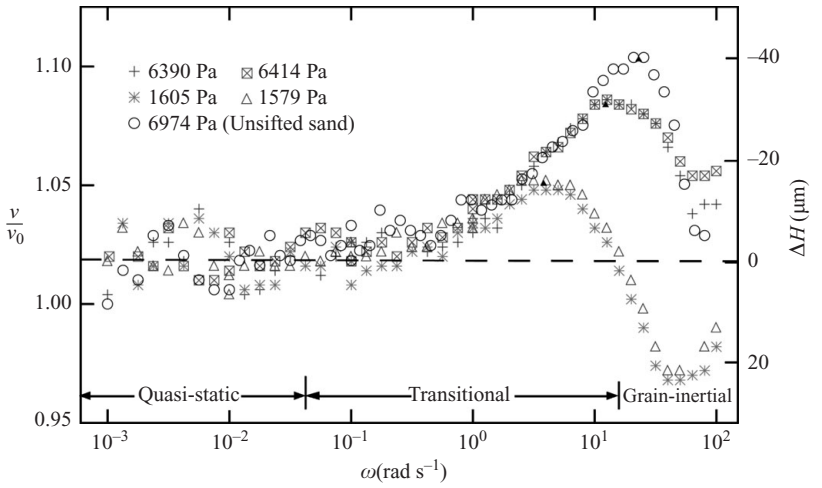

FIGURE 8. Semi-log plot of dimensionless volume-fraction, ν/ν_0, versus rotation rate; ν/ν_0 is calculated from the height measurements in Appendix B. Grain columns are approximately 6 mm. The right-hand y-axis is the observed change in height between the plates. The maximum height changes measured from low to high pressures are 15, 31 and 41 μm, respectively. The rising tails during high velocities occur because of slow system response. Note that the curves in this figure have the same general form as in figures 5 and 10 except that the y-axis is inverted (see § 5 for discussion in terms of constant compressibility).

calculated by comparing height change to the characteristic shear-band thickness, $L \approx 2D$, discussed in § 2 (see Appendix B for derivation). From the observations, the volume-fraction data can also be separated into QS, GI and transition regimes. As the mirror-image to the constant volume stress, it suggests that inverse Bagnold scaling, i.e. the quadratic rate dependence, also applies for the volume-fraction. Moreover, the different peaks in figure 8 show that volume-fraction is inversely proportional to pressure, implying the existence of granular compressibility.

Constant-pressure and constant-volume rheologies are intimately related. The extremums in applied stresses and volume-fraction in figures 5(*a*, *b*) and 8 occur at the same rotation rate (at $\omega \approx 23\,\mathrm{rad\,s^{-1}}$). Under a non-equilibrated steady state, the work done at the shearing surface dissipates completely through inelastic particle collisions. The work of surface stresses, given by $\nabla\cdot(\tilde{\boldsymbol{T}}\cdot\tilde{\mathbf{U}})$ where $\tilde{\boldsymbol{T}}$ is the total stress tensor, is directly proportional to the applied stress at the wall. Hence in figure 5(*a*, *b*), the minimum in shear and normal stresses is also the minimum in energy dissipation. Since volume inversely relates to pressure, a local minimum in stress corresponds to a local maximum in volume-fraction and vice versa. Thus in figure 8 with pressure kept constant, the maximum in volume-fraction occurs at the shearing state which corresponds to the minimum dissipation. The coincidence of extremums suggests that volume-fraction, stress and strain rate are intimately linked through an equation of state that does not allow them to vary independently. Furthermore, the stress minimum and volume-fraction maximum indicate an optimum condition for transporting and manipulating granular systems.

4.3. *Column height dependence*

Figure 9 plots shear stress versus rotation rate to compare results from 7 mm and 1 mm columns. The comparison shows the effect of inadequate sample size since the shear-band depth captured at 0.01 and 50 rad s^{-1} is 10 grain-diameters, or ≈4 mm

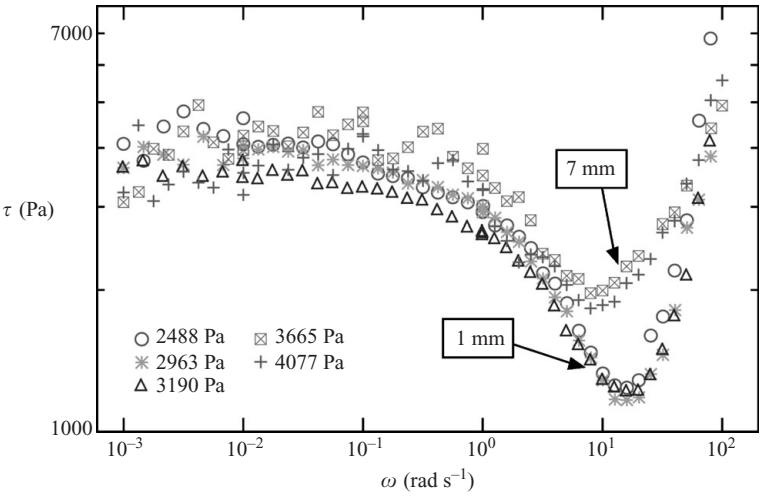

FIGURE 9. Log–log plot of shear stress versus rotation rate for constant volume (sifted sand). Plots compare results from 7 mm and 1 mm columns to show the effect of an inadequate sample volume. The shear-band depth captured at 0.01 and 50 rad s^{-1} is 10 grain-diameters, or ≈ 4 mm. Results from 1 mm columns indicate a clear distinction between QS, GI and transitional regimes.

(see § 2). Similar to the results of 7 mm columns, shear stress as a function of rate for 1 mm columns also indicates clear distinctions of QS, GI and transitional regimes.

The qualitative comparison indicates a close resemblance between QS and GI stresses from using two different column heights. The lack of grains, however, must affect the relationship between rate and stress, since the flow-depth in the 1 mm columns is much less than the observed shear-band thickness ≈ 4 mm. The granular fluid must cope with its thinner column with a higher anisotropy in force-chain orientations, as discussed in § 4.1.2. Therefore we conclude, in agreement with dimensionless analysis (see Appendix A), that the limiting regimes follow the basic frictional and inertial grain interactions, regardless of flow thickness. Yet, 1 mm flows have dissimilar shear-weakening transitions to 7 mm flows, a claim supported in § 5.1 and table 3 by the disparity between fitting coefficients.

5. Constitutive law

A key uncertainty in describing the fluid-like behaviour of granular materials is the transition between the collisional and frictional regimes. The inability of the continuum constitutive relations, such as the Navier–Stokes equation, to account for the heterogeneities of granular flow has been a difficult issue to overcome. To model the macroscopic quantities of granular mediums, such as stress, packing density or flow profile, many theories rely on the visco-plastic or elasto-plastic description used for metals (see Savage 1998; Dartevelle 2004). Although these approaches capture certain aspects of the frictional nature of granular materials by assuming perfect plasticity, they are inadequate for the results presented here. The rate dependence in stress and volume-fractions captured in figures 5 and 8 indicate the complexities of granular flow unaccounted for by the continuum models.

To capture the macroscopic effect of localized flows, we describe granular flow from analogous concepts in conventional thermodynamics. Similar to pressure, temperature

Fitting parameters	CG_{1mm}	CG_{6mm}	CF_{7kPa}	Ratio
$\beta \times 10^4$ (Pa^{-1})	15 ± 4	6.1 ± 0.4	5.9 ± 0.3	1.0
C_1	≈ 1	≈ 1	≈ 1	1.0
$C_2 \times 10^5$ (s)	19 ± 6	2.1 ± 0.8	2.5 ± 0.6	0.84
$C_3 \times 10^3$	13 ± 6	0.9 ± 0.7	2.1 ± 0.5	0.42
$\delta^\dagger$ (μm)	13	13	13	1.0

†The same value for the dilatancy volume, δ, is imposed for all experiments *a priori* to solve for ϕ in Appendix C.

TABLE 3. Summary of the fitting constants for constant-volume and constant-pressure experiments. All values are averaged amongst all experimental fits. The ratio compares the parameter fits between the 6 mm constant-volume and constant-pressure data. A ratio of unity signifies the consistency between the fitting parameters across both experiments. The $\pm$ values represent standard deviations of the parameters for the best-fit to each of the experimental runs under the given conditions. C_1 is approximately unity, but it must satisfy the constraint of $C_1 < 1$ for materials under consolidation. Averaging involves 5 runs each for 1 mm and 6 mm constant-volume experiments and 2 runs for constant-pressure experiment.

and density for describing solids and fluids, dry granular flow may be defined by pressure, deviatoric strain rate and volume-fraction (see Liu & Nagel 1998). Although granular fluids are non-thermal in the classical sense unlike molecular fluids, the minimization in gravitational potential nonetheless drives granular compaction under external excitations into energetically favourable states. Below, we develop an equation-of-state to model our results.

Our model must satisfy the shear-weakening and shear-compacting observations in figures 5(*a*, *b*) and 8. Note, the following analysis applies only to beach sand results. Quantitatively, the two rate-dependent observations from our beach sand experiments within intermediate shear rates are

$$\left(\frac{\partial \sigma}{\partial \nu}\right)_{\dot{\gamma}} > 0, \left(\frac{\partial \sigma}{\partial \dot{\gamma}}\right)_{\nu} < 0, \tag{5.1a, b}$$

where σ is normal stress, ν is solid-volume-fraction, and $\dot{\gamma}$ is shear rate. The first inequality of (5.1) is the compressible relation that describes granular shear bands. It resembles a conventional compressibility relation. The physical explanation of the second inequality in (5.1) remains unknown, yet it agrees with the scenario presented in § 4.1.2 and figure 5.

Changes in volume-fraction with respect to shear rate can be derived from (5.1*a*, *b*) using the cyclic rule,

$$\left(\frac{\partial \sigma}{\partial \nu}\right)_{\dot{\gamma}} \left(\frac{\partial \nu}{\partial \dot{\gamma}}\right)_{\sigma} \left(\frac{\partial \dot{\gamma}}{\partial \sigma}\right)_{\nu} = -1. \tag{5.2}$$

Thus similar to the thermal expansion relation – if shear rate takes on the role of temperature – volume-fraction at constant pressure relates to rate by

$$\left(\frac{\partial \nu}{\partial \dot{\gamma}}\right)_{\sigma} > 0, \tag{5.3}$$

as seen in figure 8.

To proceed, we define an observable compressibility β for the shear band within a two-phase mobilized granular system.

$$\beta \equiv \frac{1}{V}\left(\frac{\partial V}{\partial \sigma}\right)_{\dot{\gamma}}, \tag{5.4}$$

where V is the volume of the test cell. Since $V \propto \nu^{-1}$, changes in the cell volume can be mapped to changes in the solid volume fraction in the shear band, even though the total volume of the shear band cannot be measured directly. The compressibility is related to the data using the cyclic rule (5.2) as

$$\frac{1}{V}\left(\frac{\partial V}{\partial \sigma}\right)_{\dot{\gamma}} = -\frac{1}{V}\left(\frac{\partial V}{\partial \dot{\gamma}}\right)_{\sigma}\left(\frac{\partial \dot{\gamma}}{\partial \sigma}\right)_{V}. \tag{5.5}$$

Using (5.5) and the variations with strain rate of the stress (σ) and column-height (ΔH) data in figures 5 and 8, the mean granular fluid compressibility β in both quasi-static and transitional regimes is $\approx 4 \times 10^{-3}\,\mathrm{Pa}^{-1}$, independent of strain rate.

We must clarify that the actual volume change of the rigid constituent is negligible under low to moderate pressure, i.e. $\sigma \ll E$, where E is the grain elastic modulus. Therefore, the compressible nature of granular flow is solely due to the volumetric changes in the interstitial spaces. In a crystalline solid, the physical interpretation of β lies in the second derivative of lattice potential per molecule with respect to lattice spacing. In granular flow, however, the physical origin of β is not yet understood.

Also, the compressibility is distinctly different from the irreversible process of granular consolidation (see Nedderman 1992; Nowak *et al.* 1997). For both static and dynamic granular systems, consolidation irreversibly reduces void fraction. Here, in contrast, we assume the changes in volume-fraction are entirely reversible. In this context, the term reversible does not imply an isentropic process as in classical thermodynamics. Figure 8 shows volumetric reversibility as the same medium contracts and expands across a maximum volume-fraction.

To develop a constitutive law from a free-volume analysis, we now define an effective interstitial free-volume fraction e. Up to and excluding the GI deformation rates, the compressibility of a mobilized granular solid in terms e, at constant, non-zero shear rate is

$$\left[\frac{1}{e}\frac{\partial e}{\partial \sigma_{QS}}\right]_{\dot{\gamma}} = -\beta \quad \text{for} \quad \beta \geqslant 0, \tag{5.6}$$

where σ_{QS} is the contribution to the isotropic compressive stress in the QS and transitional regimes. (The GI contribution is added later in (5.21).) The interstitial void fraction, e, is defined as the ratio between the expanded 'free' volume, which allows for grain mobilization, to the bulk static volume (see figure 1). It is equal to zero for a static packing, but it has a finite value for a network of moving grains; e relates to the granular volume-fraction ν as

$$\nu = \frac{\nu_\infty}{1+e}, \quad e = \frac{\nu_\infty - \nu}{\nu}, \quad e \geqslant 0, \tag{5.7}$$

and ν_∞ is the maximum volume-fraction during steady-state shear as a function of maximum pressure and minimum shear rate. The effective void fraction is also a measure of grain mobility within a dense packing. Integrating (5.6) at constant compressibility and substituting into (5.7) at a constant shear rate $\dot{\gamma}$, yields

$$\sigma_{QS}(\nu) = -\frac{1}{\beta}\left[\ln(e) + const\right] = \frac{1}{\beta}\left[\ln\left(\frac{\nu}{\nu_\infty - \nu}\right) + const\right]. \tag{5.8}$$

Separating the integration constant into rate-independent and rate-dependent parts A and $B(\dot{\gamma})$, respectively, (5.8) becomes

$$\sigma_{QS}(\nu, \dot{\gamma}) = \frac{1}{\beta}\left[\ln\left(\frac{\nu}{\nu_\infty - \nu}\right) + A + B(\dot{\gamma})\right]. \tag{5.9}$$

To solve for the unknowns in (5.9), we use the inequalities in (5.1) to formulate the effect of volume-fraction on pressure and shear rate. From observation, volume-fraction ν has the following boundary conditions for the QS component:

$$\nu = \nu_0' \quad \text{as} \quad \sigma \to 0, \dot{\gamma} \to 0, \tag{5.10a}$$

$$\nu = \nu_\infty' \quad \text{as} \quad \sigma \to 0, \dot{\gamma} \to \infty, \tag{5.10b}$$

$$\nu = \nu_\infty \quad \text{as} \quad \sigma \to \infty, \dot{\gamma} \to \infty, \tag{5.10c}$$

where ν_0' and ν_∞' are the maximum and minimum volume-fractions at the limit of zero applied load, respectively, and ν_∞ is the theoretical maximum dynamic volume-fraction. However, in actuality for the current experiment, ν_0' and ν_∞' are the respective absolute maximum and minimum volume-fractions for systems under gravity. For comparison, $\nu_0' < \nu_\infty' \leqslant \nu_\infty$ and all of them are quantities measured in a mobilized particle system. Note, although there is no absolute minimum packing under zero applied stress, gravity enforces the lower limit on volume-fraction in our experiment. Using boundary condition (5.10*b*), (5.9) becomes for $\dot{\gamma} \to \infty$

$$\frac{1}{\beta}\left[\ln\left(\frac{\nu_\infty'}{\nu_\infty - \nu_\infty'}\right) + A + B\,(\dot{\gamma})\right] = 0 \tag{5.11}$$

and if B($\dot{\gamma} \to \infty$)=0, then

$$A = \ln\left(\frac{\nu_\infty - \nu_\infty'}{\nu_\infty'}\right).$$

From here, (5.9) becomes

$$\sigma_{QS}(\nu, \dot{\gamma}) = \frac{1}{\beta}\left[\ln\left(\frac{\nu_\infty - \nu_\infty'}{\nu_\infty - \nu}\right)\left(\frac{\nu}{\nu_\infty'}\right) + B(\dot{\gamma})\right] \cong \frac{1}{\beta}\left[\ln\left(\frac{\nu_\infty - \nu_\infty'}{\nu_\infty - \nu}\right) + B(\dot{\gamma})\right], \tag{5.12}$$

where the approximation is applicable if volume-fraction changes are small so that the $\nu/\nu_\infty' \approx 1$. We assume that the volume-fraction is exponentially dependent on strain rate with fitting constants C_1 and C_2, while satisfying the boundary conditions. According to shear-compaction in (5.3), the volume-fraction increases with shear rate of the form

$$\nu(\sigma, \dot{\gamma}) = \nu_\infty - \frac{\nu_\infty - \nu_\infty'}{1 - C_1 \exp(-C_2\dot{\gamma})} func(\sigma_{QS}), \tag{5.13}$$

where $func(\sigma_{QS})$ is an arbitrary stress function to make the equation self-consistent with (5.12). Note, the rigorous derivation of the exponential function of shear rate is not included in the current derivation. The physical meaning of $C_2 = fn(\rho U^2/\sigma, \mu_f, \nu, e, s)$ may be the consolidation time τ_c given in Appendix A.4. The ratio $\tau_c/\dot{\gamma}^{-1}$ would then compare grain-settling time to grain-contact time. A larger τ_c describes a denser medium at a given pressure and particle density, where grains move sluggishly into neighbouring vacancies.

Substituting for ν using (5.13), (5.12) becomes

$$\frac{\nu_\infty - \nu_\infty'}{\nu_\infty - \nu} = \frac{1 - C_1 \exp(-C_2\dot{\gamma})}{func(\sigma_{QS})} = \exp[\beta\sigma_{QS} - B(\dot{\gamma})] \tag{5.14}$$

and solving for $func(\sigma_{QS})$ and $B(\dot{\gamma})$, we obtain

$$func(\sigma_{QS}) = \exp(-\beta\sigma_{QS}) \tag{5.15}$$

and

$$\exp[B(\dot{\gamma})] = \frac{1}{1 - C_1 \exp(-C_2\dot{\gamma})}. \tag{5.16}$$

Then using (5.15), (5.13) becomes

$$\nu(\dot{\gamma}, \sigma_{QS}) = \nu_\infty - \frac{\nu_\infty - \nu'_\infty}{1 - C_1 \exp(-C_2\dot{\gamma})} \exp(-\beta\sigma_{QS}). \tag{5.17}$$

For completeness, by applying boundary condition (5.10*a*), the gravity-induced minimum volume-fraction is

$$\nu(\dot{\gamma} \to 0, \sigma \to 0) = \nu'_0 = \nu_\infty - \frac{\nu_\infty - \nu'_\infty}{1 - C_1} \tag{5.18}$$

and

$$\nu'_\infty/\nu_\infty \leqslant C_1 < 1, \tag{5.19}$$

since $\nu \geqslant 0$ and $\nu \leqslant \nu'_\infty < \nu_\infty$. The magnitude of C_1 is a function the compacting forces, i.e. external pressure or gravity. As the rate approaches zero, the limiting volume fraction ν'_0 under zero gravity is referred to by Onoda & Liniger (1990) as the 'dilatancy onset' – a particular packing-density where shear-dilatancy does not occur. From (5.17), the bulk stress of a granular solid is

$$\sigma_{QS}(\nu, \dot{\gamma}) = \frac{1}{\beta} \ln \left[\frac{\nu_\infty - \nu'_\infty}{\nu_\infty - \nu} \frac{1}{1 - C_1 \exp(-C_2\dot{\gamma})} \right]. \tag{5.20}$$

Notice (5.20) accounted only for the states within the QS and the transitional regimes. To include the GI regime fit, we looked at the dimensionless groups of (A 5) where the stresses are quadratically dependent on shear rate. Therefore, similar to the Savage (1998) analysis, the GI stress is

$$\sigma_{GI} = func(\nu, e, s)\rho D^2\dot{\gamma}^2 = C_3\rho D^2\dot{\gamma}^2. \tag{5.21}$$

Here, the function term is reduced to a fitting constant C_3 since the sample and volume-fraction are kept constant in the experiment. Summing (5.20) and (5.21), we form a constitutive law for the observations in figures 5(*a*, *b*) and 8, namely,

$$\sigma_{sum}(\nu, \dot{\gamma}) = \frac{1}{\beta} \ln \left[\frac{\nu_\infty - \nu'_\infty}{\nu_\infty - \nu} \frac{1}{1 - C_1 \exp(-C_2\dot{\gamma})} \right] + C_3\rho D^2\dot{\gamma}^2. \tag{5.22}$$

As for shear stress, by assuming a constant proportionality that $\mu = \tau/\sigma$, it becomes clear that

$$\tau_{sum}(\nu, \dot{\gamma}) = \mu \left\{ \frac{1}{\beta} \ln \left[\frac{\nu_\infty - \nu'_\infty}{\nu_\infty - \nu} \frac{1}{1 - C_1 \exp(-C_2\dot{\gamma})} \right] + C_3\rho D^2\dot{\gamma}^2 \right\}. \tag{5.23}$$

Also, a composite volume-fraction ϕ that relates to the ratio of the interstitial volumes e and e'_∞ is given by

$$\phi = \frac{e'_\infty}{e} \approx \frac{\nu_\infty - \nu'_\infty}{\nu_\infty - \nu}. \tag{5.24}$$

The interstitial free-volume ratio e and the minimum ratio e'_∞, which is applicable as the rate approaches infinity, are based on (5.7). Appendix C calculates the experimental

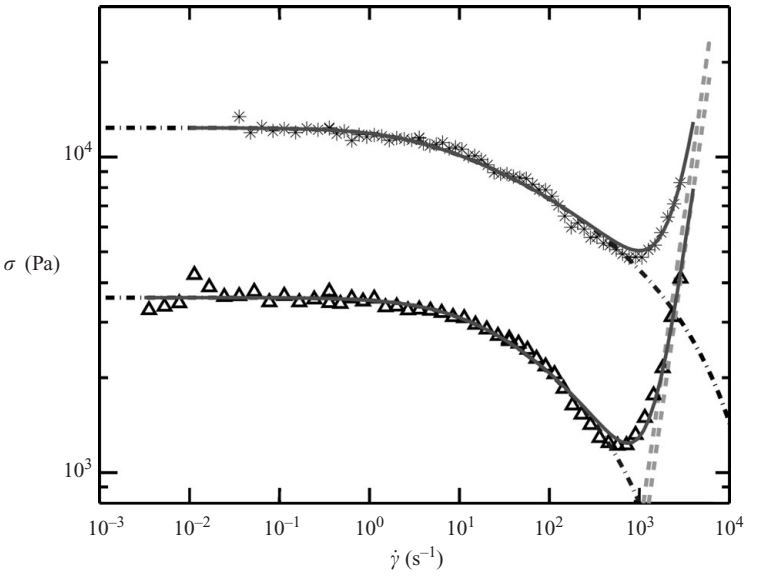

FIGURE 10. Log–log plot comparing data and the model for pressure versus shear rate from the constant-volume experiments. The fit has two sets for Δ, 1 mm and *, 6 mm experiments. –·–, QS fit (5.20); – – –, GI fit (5.21); ——, the sum of the previous two contributions (see (5.22)). Other results totalling 5 runs each from 6 mm and 1 mm experiments show consistent fits.

ϕ based on the measured height change. Thus, (5.22) can be written as

$$\phi = [1 - C_1 \exp(-C_2\dot{\gamma})] \exp[\beta(\sigma_{sum} - C_3\rho D^2\dot{\gamma}^2)]. \tag{5.25}$$

5.1. *Least-squares fit*

In figure 10, the log–log plot fits (5.22) to the constant-volume experiment in figure 5(*b*). The pressure versus strain-rate data are for sifted beach sand. The log–log plot shows the stress contribution from the GI factors in (5.21) and the QS factors in (5.20) separately, and their sum is in good agreement with the observed flow regimes. In figure 11, the log–log plot fits (5.25) to the constant-pressure experiment in figure 8. The interstitial volume ratio ϕ , as given in (5.24), is found using the measured column height with the method described in Appendix C.

The constants β, C_1, C_2 and C_3 are found using an iterative least-squares fitting procedure in MATLAB. Table 3 gives the fitting constants for experiments of 1 μm and 6 μm columns as well as constant-volume and constant-pressure configurations. The resulting fits correlate well only for the 6 mm experiments. The coefficients for 1 mm parameters are significantly different from the 6 mm fits. The disparity indicates the lack of scale invariance with respect to system size for the fitting parameters β, C_1, C_2 and C_3. Thus based on the lack of consistency, we speculate that our constants are only consistent for sufficiently large sample volumes (see § 4.3).

Table 3 summarizes our fitting results. The *a priori* value of 13 μm is used for the dilatancy height δ in (C 5) to calculate the interstitial volume ratio ϕ for all fits. Compressibility β can be compared to the mean value $\approx 4\times10^{-3}$ Pa^{-1} measured from (5.5) using stress-rate and volume-rate data. The similar values in both fit and model confirm the compressible nature of granular fluids. Constant C_1 is nearly unity; it is restricted to be less than 1 in the fitting procedure, as required for the non-negative

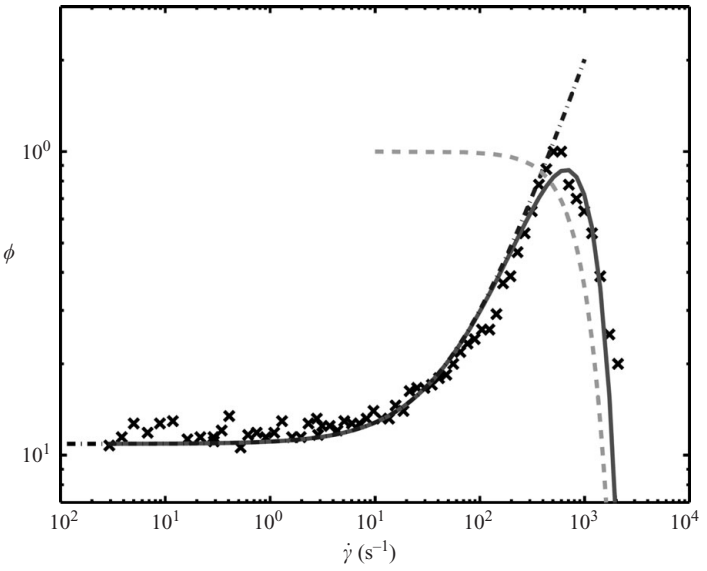

FIGURE 11. Log–log plot of comparison between theory and free-volume ratio versus shear rate from the constant-pressure experiment. $\times$, $\sigma = 7$ kPa. The grain column is 6 mm. $-\cdot-$, QS fit; $---$, GI fit; ——, the product of the previous two contributions as shown in (5.25).

volume-fraction as derived in (5.19). C_1 determines the solid volume-fraction at the 'dilatancy onset' (see Onoda & Liniger 1990) and it is a positive function of the consolidation pressure. Constant C_2 is $\sim 10^{-5}$ s, and for the parameters in table 1, the settling time τ_c is $\sim 10^{-4}$ s from (A 7). The near-coincidence of these values suggests a line of investigation for further work. Constant C_3 is a function of volume-fraction according to (A 5) and the analysis by Savage (1998). The slight inconsistency between constant-volume and constant-pressure values of C_3 in table 3 support this claim.

The agreement between our analytical model and empirical data from both heights, along with similar fitting parameters, validates the present model. The compressibility of air at standard temperature and pressure (STP) condition is 10^{-5} Pa^{-1}, about one order of magnitude less than the compressibility of flowing sand.

6. Conclusions

In our attempt to recover the transitional granular flow regime, we have seen a glimpse of how particles collectively respond to simple shear. The five decades of shear rate in the present experiment correlate to many natural and industrial processes: avalanches, landslides, dredging and particle fluidization in mixing, segregation and compaction. Our results show the following.

(i) During constant volume, shear-weakening occurs during transitional flow rates. Both shear and normal stresses 'dip' and reach a minimum value. Bagnold scaling $\sim \dot{\gamma}^2$ is observed for the grain-inertial regime.

(ii) During constant pressure, shear-compaction occurs during transitional flow rates. The reversible volume-fraction plateaus and then decreases with inverse Bagnold scaling $\sim \dot{\gamma}^{-2}$ in the grain-inertial regime.

(iii) The transitional flow regime is much broader than previous observations spanning a Savage number range from 10^{-7} to 10^{-1}.

(iv) An equation-of-state devised based on granular compressibility unifies our findings. Fitting parameters remain consistent from all experiments with adequate shear-band thickness.

(v) Particle sphericity has a great effect on transitional regime. Shear-weakening does not exist for spherical grains, only rate-independent Coulomb stresses that preceed Bagnold stresses $\sim \dot{\gamma}^2$ above a Savage number ~ 1.

The present constitutive law provides insight into the scenario presented in § 4.1.2 illustrating a plausible physical origin for the observed granular rheology. As the strain rate increases in a dense flow, force chains collapse and the granular fluid becomes less stiff. The weaker fluid requires smaller normal forces to maintain the packing imposed by the constant-volume boundary conditions. The result is the 'dip' that is observed in our experiments.

The quantitative analysis has its shortcomings. In particular, it does not consider material properties such as the coefficient of restitution, rigidity and contact friction. We do, however, suspect inelastic collisions, as well as boundary effect, to be a part of a separate conservation law that balances the inter-granular momentum and energy (see Jop *et al.* 2005), a law of motion that resolves velocity profile, granular temperature, dissipation and convection (see Knight *et al.* 1996).

Despite being an incomplete description of granular flow, the current model delineates granular-flow regimes. Moreover, the compressible model formulated for the transitional regime may reflect the emerging macroscopic effect of the self-organizational network of force chains. Although the local contact forces and volume-fraction are highly probabilistic (see Behringer *et al.* 1999), spatial and temporal ensemble averaging of the physical quantities provides a deterministic granulodynamics as indicated by our experiment.

We hope the presented model can predict granular rheology in other configurations. A non-trivial extension, however, is required in order to account for disparate methods of excitation. The shear-driven deformation in our case is unlike gas or vibration-induced fluidization. It will be interesting to see a comparison with the results from a chute flow or fluidized bed. The comparison may further elucidate the exact physical meanings of the fitting constants C_1, C_2, C_3 used in our equations. The difficult interpretation of the heterogeneous shear band must be reconciled in the various flow types.

Our future work also includes a new annulus set-up. A confined channel will help to eliminate any possible effect biased to the shear-rate variation of our current set-up. Material confinement and excessive wear are the difficulties to overcome for the current annulus geometry. Preliminary results show good agreement with the present flat-plate configuration.

Appendix A. Dimensionless analysis

A general function for the macroscopic granular flow shear stress in terms of other independent variables is

$$\tau = fn(\sigma, \rho, U, g, \nu, D, D', e, \mu_f, E, s). \tag{A 1}$$

where σ is the applied pressure, ρ is the solid density, U is the translational grain velocity, D is the average grain diameter, D' is the sample size variance, or the degree of polydispersity, g is the acceleration due to gravity, e is the coefficient of restitution defined as the ratio between incident and reflected velocities, ν is the bulk solid volume-fraction, μ_f is the intergrain friction coefficient, E is the bulk elastic modulus

of the material and s is the grain sphericity which affects inter-particle friction. Equation (A 1) is similar to that offered by Savage (1984). Since shear bandwidth is proportional to grain size, the fluidized shear thickness is implicitly included in the analysis. Below we quantify each regime using the Buckingham Pi theorem.

A.1. *Quasi-static regime*

To understand the pertinent parameters within the quasi-static regime, we choose applied pressure σ, particle density ρ, and gravity g to quantify the flow. Thus, (A 1) in terms of dimensionless groups for the quasi-static regime is

$$\frac{\tau}{\sigma} = fn\left(\frac{\rho U^2}{\sigma}, \frac{\rho g D}{\sigma}, \frac{\rho g D'}{\sigma}, \frac{E}{\sigma}, \mu_f, \nu, e, s\right). \tag{A 2}$$

In our analysis for large applied loads, the gravitational body forces can be neglected in (A 2). The particle Young's modulus, E, is also assumed to be sufficiently high compared to the applied pressure, σ. Also, because of segregation, $D' \ll D$. From the above assumptions, for vanishing shear velocity and thus neglecting inelastic collision effects, (A 2) becomes

$$\frac{\tau}{\sigma} = fn(\mu_f, \nu, s). \tag{A 3}$$

The resulting stress behaviour is only a function of particle friction and sphericity, and volume-fraction. The overall macroscopic properties are also rate-independent for a granular layer operating in the quasi-static regime. The effect of grain sphericity s may tie directly into volume-fraction, as discussed in § 3.

A.2. *Grain-inertial regime*

In a rapid shear flow, instead of a frictional sliding contact between grains, it is the inelastic collisions that are responsible for most of the momentum transport. The solid concentration is low and particles have a random fluctuation velocity component in addition to the mean velocity (see Savage 1984). For the GI regime, we choose ρ, D and U to quantify the flow. Thus, (A 1) in its dimensionless groups for Savage numbers greater than unity becomes

$$\frac{\tau}{\rho U^2} = fn\left(\frac{\sigma}{\rho U^2}, \frac{D'}{D}, \frac{E}{\rho U^2}, \frac{gd}{U^2}, \mu_f, \nu, e, s\right). \tag{A 4}$$

Analogous to the procedure in § A.1, the particle-kinetic quality of granular material is revealed by neglecting gravitational and lower-order velocity terms in (A 4). Also because of segregation, the medium becomes mono-dispersed circumferentially so that $D' \ll D$. The resulting mean shear and normal stresses, τ and σ, are described as

$$\frac{\tau}{\rho U^2} = fn\left(\frac{\sigma}{\rho U^2}, \nu, e, s\right). \tag{A 5}$$

Stresses are proportional to the square of the average grain velocity, or the granular kinetic energy. Equation (A 5) is comparable to the relations given in Bagnold's analysis (1954).

A.3. *Transitional flow regime*

In the limiting flow regimes discussed above, bulk stresses are controlled by different mechanisms and physical parameters as mentioned in Appendices A.1 and A.2. Therefore, the transitional regime between them should consequently exhibit features that resemble both rate-dependent and rate-independent regimes. Depending on the

relative stress levels and packing density and assuming the compressible nature of granular packing density, various dimensionless groups in (A 3) and (A 5) can be significant. We anticipate the importance of first-order velocity to the quasi-static groups. Hence,

$$\frac{\tau}{\sigma} = fn\left(\frac{\rho U^2}{\sigma}, \mu_f, \nu, e, s\right). \tag{A 6}$$

A.4. *Consolidation time scale*

The settling or relaxation time for granular fluids under pressure can be approximated from kinematics as $\tau_c \sim \sqrt{2l/\bar{a}}$. Length scale $l \sim D$, the mean grain diameter, represents the vacancy length per grain that allows for grain mobility, as a direct result of shear-dilation–interstitial volume expansion due to granular deformation (see Reynolds 1885). It resembles the length scale Bagnold derived from solid volume-fraction (see Bagnold 1954). Average grain acceleration $\bar{a}$ from wall collisions relates to the vacancy length, consolidation pressure σ, and grain density ρ by $\bar{a} \sim \sigma/\rho l$. Similarly for grains rotating from wall shear, angular acceleration becomes $\bar{\alpha} \sim \tau/\rho Dl$ where $\bar{\alpha} \sim \bar{a}/D$. These rough estimates also assume Hertzian contact area as $\sim D^2$ from a rough shearing surface. Finally since $l \sim D$ and $\sigma \sim \tau$, we arrive at an average relaxation time,

$$\tau_c \sim D\sqrt{\frac{\rho}{\sigma}}. \tag{A 7}$$

The time scale (A 7) refers to how fast grains settle into their respective vacancies under compression. It implicitly assumes that it is only for dense flows, so that $l \sim D$ becomes small to a degree where the system no longer consolidates relative to the experimental time scale $\sim \dot{\gamma}^{-1}$. It is at this dense packing where the system can approach steady-state shear. Also note for extremely low shear rates, the above analysis is valid only for angular grain mixtures where crystallization – the ordered packing of a lattice formation – is bypassed. See § 4.1.2 for a detailed discussion.

Appendix B. Dimensionless volume-fraction

The relations below approximate the volume-fraction ratio ν/ν_0, where ν_0 is the volume-fraction during the QS regime as the shear rate approaches zero. For an arbitrary shear-band thickness H_α and area A, the mass of the sample bulk is

$$[mass]_\alpha = \rho \nu_\alpha H_\alpha A, \tag{B 1}$$

and ρ and ν_α are material density and volume-fraction. For the same number of particles, the total mass remains constant through any volumetric changes. Then for a different shear-band thickness H_β,

$$\nu_\alpha H_\alpha = \nu_\beta H_\beta, \quad H_\alpha(\dot{\gamma}) = H_\beta + \Delta H(\dot{\gamma}), \tag{B 2}$$

where $\Delta H(\dot{\gamma}) > 0$ is the height change – the only measured parameter. The rate-dependent H_β conflicts with our Savage-number approximation where shear-band thickness is assumed to be rate invariant. The inconsistency may be explained by figure 8 where the maximum $\Delta H(\dot{\gamma})$ is below the resolution of a single grain – hence

$\Delta H(\dot{\gamma})$ does not alter our approximation that $H \approx 2D$. Continuing from (B 2), the dimensionless volume-fraction becomes

$$\frac{\nu_\alpha}{\nu_\beta} = 1 + \frac{\Delta H}{H_\beta}. \tag{B 3}$$

Shear-band thickness H_β and its corresponding volume-fraction ν_β are based on the first-order approximation of the shear thickness being $\approx 2D$, as discussed in § 2. For clarification, $\nu = \nu_{static}$ outside the shear band where grains are statically packed. Using consistent indices by transforming $\alpha \to 0$ as the initial QS height, (B 3) becomes

$$\frac{\nu(\dot{\gamma})}{\nu_0} = 1 + \frac{\Delta H(\dot{\gamma})}{2D} > 1. \tag{B 4}$$

Appendix C. Free-volume ratio

To compare our model to the experimental data, the free-volume ratio ϕ in (5.25) is calculated for constant-pressure experiments. Since the volume-fraction is impossible to measure during shear, the measured top-plate height H is used instead. For a given volume of porous material with unconfined height, the overall volume-fraction is inversely proportional to the column height and a reference height. Here, we choose the absolute maximum volume-fraction and its corresponding column height, explicitly as ν_∞ and H_1 (figure 1). Therefore,

$$\nu = \frac{\nu_\infty H_1}{H}, \quad \nu'_\infty = \frac{\nu_\infty H_1}{H_2}, \tag{C 1}$$

where ν_∞ and ν'_∞ represent the dynamic volume-fractions as given in the boundary conditions in (5.10*a*)–(5.10*c*). Note, ν'_∞ is a state variable and thus non-universal. H_1 and H_2 are the associated column heights for each volume-fraction, ν_∞ and ν'_∞, signifying the dilation process during granular fluidization. The relationship between H_1, H_2 and $H(\dot{\gamma})$ is

$$H(\dot{\gamma}) = H_2 + \Delta H(\dot{\gamma}) = H_1 + \delta + \Delta H(\dot{\gamma}), \tag{C 2}$$

where δ is the 'dilatancy height' that defines the minimum height difference between dynamic and static packing (see figure 1). $\Delta H(\dot{\gamma})$ is the measured column height change by the system. For comparison, $H_1 < H_2 < H_3$. Therefore, the volume-fraction ratio from (5.25), using (C 1), is

$$\frac{\nu_\infty - \nu'_\infty}{\nu_\infty - \nu} = \frac{1 - H_1/H_2}{1 - H_1/H}, \tag{C 3}$$

and combine with relation (C 2),

$$\frac{\nu_\infty - \nu'_\infty}{\nu_\infty - \nu} = \frac{1 - H_2/H_2 + \delta/H_2}{1 - H(\dot{\gamma})/H(\dot{\gamma}) + \delta/H(\dot{\gamma}) + \Delta H(\dot{\gamma})/H(\dot{\gamma})}. \tag{C 4}$$

Also assuming $H_2 \approx H(\dot{\gamma})$, the interstitial volume ratio ϕ becomes

$$\phi = \frac{\nu_\infty - \nu'_\infty}{\nu_\infty - \nu} \cong \left(1 + \frac{\Delta H(\dot{\gamma})}{\delta}\right)^{-1} \leqslant 1. \tag{C 5}$$

REFERENCES

Aharonov, E. & Sparks, D. 2004 Stick-slip motion in simulated granular layers. *J. Geophys. Res.-Solid Earth*, **109**.

Bagnold, R. A. 1954 Experiments on a gravity free dispersion of large solid spheres in a Newtonian fluid under shear. *Proc. R. Soc. Lond.* A **225**, 49–63.

Behringer, R. P., Howell, D., Kondic, L., Tennakoon, S. & Veje, C. 1999 Predictability and granular materials. *Physica* D **133**, 1–17.

Bocquet, L., Losert, W., Schalk, D., Lubensky, T. C. & Gollub, J. P. 2002 Granular shear flow dynamics and forces: experiment and continuum theory. *Phys Rev* E **65** (1), 011307.

Bossis, G., Grasselli, Y. & Volkova, O. 2004 Granular rheology in zero gravity. *J. Phys. Cond. Matter* **16**, 3279–3287.

Campbell, C. S. 1990 Rapid granular flows. *Annu. Rev. Fluid Mech.* **22**, 57–92.

Campbell, C. S. 2002 Granular shear flows at the elastic limit *J. Fluid Mech.* **465**, 261–291.

Campbell, C. S. 2005 Stress-controlled elastic granular shear flows. *J. Fluid Mech.* **539**, 273–297.

Campbell, C. S. 2006 Granular material flows – an overview. *Powder Technol.* **162**, 208–229.

Cates, M. E., Wittmer, J. P., Bouchaud, J. P. & Claudin, P. 1999 Jamming and static stress transmission in granular materials. *Chaos* **9**, 511–522.

Cheng, D. C. H. & Richmond, R. A. 1978 Some observations on rheological behavior of dense suspensions. *Rheol. Acta* **17**, 446–453.

Corwin, E. I., Jaeger, H. M. & Nagel, S. R. 2005 Structural signature of jamming in granular media. *Nature* **435**, 1075–1078.

da Cruz, F., Emam, S., Prochnow, M., Roux, J. N. & Chevoir, F. 2005 Rheophysics of dense granular materials: discrete simulation of plane shear flows. *Phys. Rev.* E **72**, part 1 021309.

Dalton, F., Farrelly, F., Petri, A., Pietronero, L., Pitolli, L. & Pontuale, G. 2005 Shear stress fluctuations in the granular liquid and solid phases. *Phys. Rev. Lett.* **95** (13).

Dartevelle, S. 2004 Numerical modeling of geophysical granular flows: 1. a comprehensive approach to granular rheologies and geophysical multiphase flows. *Geochem. Geophys. Geosyst.* **5**.

Drake, T. G. 1990 Structural features in granular flows. *J. Geophys. Res.* **95** (B6), 8681–8696.

Duran, J. 1999 *Sands, Powders and Grains : An Introduction to the Physics of Granular Materials*, 1st edn. Springer.

de Gennes, P. G. 1999 Granular matter: a tentative view. *Rev. Mod. Phys.* **71**, S374–S382.

Hanes, D. M. & Inman, D. L. 1985 Observations of rapidly flowing granular-fluid materials. *J. Fluid Mech.* **150**, 357–380.

Hendy, S. C. 2005 Towards a theory of granular plasticity. *J. Engng Math.* **52**, 137–146.

Howell, D. W., Behringer, R. P. & Veje, C. T. 1999 Fluctuations in granular media. *Chaos* **9**, 559–572.

Hsiau, S. S. & Shieh, Y. M. 2000 Effect of solid fraction on fluctuations and self-diffusion of sheared granular flows. *Chem. Engng Sci.* **55**, 1969–1979.

Jaeger, H. M., Nagel, S. R. & Behringer, R. P. 1996 Granular solids, liquids, and gases. *Rev. Mod. Phys.* **68**, 1259–1273.

Jop, P., Forterre, Y. & Pouliquen, O. 2005 Crucial role of sidewalls in granular surface flows: consequences for the rheology. *J. Fluid Mech.* **541**, 167–192.

Jop, P., Forterre, Y. & Pouliquen, O. 2006 A constitutive law for dense granular flows. *Nature* **441**, 727–730.

Karion, A. & Hunt, M. L. 1999 Energy dissipation in sheared granular flows. *Trans. ASME C: J. Heat Transfer* **121**, 984–991.

Kavehpour, H. P. & McKinley, G. H. 2004 Tribo-rheometry: from gap-dependent rheology to tribology. *Tribol. Lett.* **17**, 327–335.

Klausner, J. F., Chen, D. M. & Mei, R. W. 2000 Experimental investigation of cohesive powder rheology. *Powder Technol.* **112**, 94–101.

Knight, J. B., Ehrichs, E. E., Kuperman, V. Y., Flint, J. K., Jaeger, H. M. & Nagel, S. R. 1996 Experimental study of granular convection. *Phys. Rev.* E **54**, 5726–5738.

Larson, D. G. 1999 *The Structure and Rheology of Complex Fluids*. Oxford University Press.

Liu, A. J. & Nagel, S. R. 1998 Nonlinear dynamics – jamming is not just cool any more. *Nature* **396**, 21–22.

Lois, G., Lemaitre, A. & Carlson, J. M. 2005 Numerical tests of constitutive laws for dense granular flows. *Phys. Rev.* E **72**, 051303.

Majmudar, T. S. & Behringer, R. P. 2005 Contact force measurements and stress-induced anisotropy in granular materials. *Nature* **435**, 1079–1082.

Makse, H. A., Havlin, S., King, P. R. & Stanley, H. E. 1997 Spontaneous stratification in granular mixtures. *Nature* **386**, 379–382.

MiDi, G. D. R. 2004 On dense granular flows. *Eur. Phys. J.* E **14**, 341–365.

Nedderman, R. M. 1992 *Static and Kinematics of Granular Materials*, 1st edn. Cambridge University Press.

Nowak, E. R., Knight, J. B., Povinelli, M. L., Jaeger, H. M. & Nagel, S. R. 1997 Reversibility and irreversibility in the packing of vibrated granular material. *Powder Technol.* **94**, 79–83.

O'Hern, C. S., Langer, S. A., Liu, A. J. & Nagel, S. R. 2001 Force distributions near jamming and glass transitions. *Phys. Rev. Lett.* **86**, 111–114.

O'Hern, C. S., Silbert, L. E., Liu, A. J. & Nagel, S. R. 2003 Jamming at zero temperature and zero applied stress: The epitome of disorder. *Phys. Rev.* E **68** (1), 011306.

Onoda, G. Y. & Liniger, E. G. 1990 Random loose packings of uniform spheres and the dilatancy onset. *Phys. Rev. Lett.* **64**, 2727–2730.

Ostojic, S., Somfai, E. & Nienhuis, B. 2006 Scale invariance and universality of force networks in static granular matter. *Nature* **439**, 828–830.

Reynolds, O. 1885 On the dilatancy of media composed of rigid particles in contact. *Phil. Mag.* **5**, 469–481.

Savage, S. B. 1984 The mechanics of rapid granular flows. *Adv Appl. Mech.* **24**, 289–366.

Savage, S. B. 1998 Analyses of slow high-concentration flows of granular materials. *J. Fluid Mech.* **377**, 1–26.

Savage, S. B. & Sayed, M. 1984 Stresses developed by dry cohesionless granular-materials sheared in an annular shear cell. *J. Fluid Mech.* **142**, 391–430.

Savage, S. B., Nedderman, R. M., Tuzun, U. & Houlsby, G. T. 1983 The flow of granular-materials3. Rapid shear flows. *Chem. Engng Sci.* **38**, 189–195.

Sawyer, W. G. & Tichy, J. A. 2001 Lubrication with granular flow: continuum theory, particle simulations, comparison with experiment. *Trans. ASME J. Tribol.* **123**, 777–784.

Shinbrot, T. 2004 Granular materials – the brazil nut effect – in reverse. *Nature* **429**, 352–353.

Tardos, G. I., Khan, M. I. & Schaeffer, D. G. 1998 Forces on a slowly rotating, rough cylinder in a couette device containing a dry, frictional powder. *Phys. Fluids* **10**, 335–341.

Tardos, G. I., McNamara, S. & Talu, I. 2003 Slow and intermediate flow of a frictional bulk powder in the Couette geometry. *Powder Technol.* **131**, 23–39.

Tuzun, U., Houlsby, G. T., Nedderman, R. M. & Savage, S. B. 1982 The flow of granular-materials2. Velocity distributions in slow flow. *Chem. Engng Sci.* **37**, 1691–1709.

Visscher, W. M. & Bolsterl, M. 1972 Random packing of equal and unequal spheres in 2 and 3 dimensions. *Nature* **239**, 504–508.

Yu, A. B., Zou, R. P. & Standish, N. 1996 Modifying the linear packing model for predicting the porosity of nonspherical particle mixtures. *Indust. Engng Chem. Res.* **35**, 3730–3741.

Zou, R. P. & Yu, A. B. 1996 Evaluation of the packing characteristics of mono-sized non-spherical particles. *Powder Technol.* **88**, 71–79.